

Optical spectral weight: comparison of weak and strong spin-orbit coupling

Zhou Li^{1,3,4*} and J. P. Carbotte^{1,2†}

¹ *Department of Physics, McMaster University, Hamilton, Ontario Ontario, Canada, L8S 4M1*

² *Canadian Institute for Advanced Research, Toronto, Ontario, Canada M5G 1Z8*

³ *Department of Physics and Astronomy, Louisiana State University, Baton Rouge, LA, 70803 USA*

⁴ *Center for Computation and Technology, Louisiana State University, Baton Rouge, LA, 70803 USA*

(Dated: March 10, 2015)

The Fermi velocity (v_F) associated with the spin-orbit coupling is two orders of magnitude smaller for spintronic semiconductors than it is for topological insulators. Both families can be treated with the same Hamiltonian which contains a relativistic (Dirac) linear in momentum term proportional to v_F and a non-relativistic quadratic contribution with Schrödinger mass (m). We find that the AC dynamic longitudinal and transverse (Hall) magneto-conductivities are strongly dependent on the size of v_F . When the Dirac fermi velocity is small, the absorption background provided by the interband optical transitions is finite only over a very limited range of photon energies as compared with topological insulators. Its onset depends on the value of the chemical potential (μ) and on the magnetic field (B), as does its upper cut off. Within this limited range its magnitude is however constant and has the same magnitude of $e^2\pi/(8h)$ as is found in topological insulators and also in graphene noting a difference in degeneracy factor. The total optical spectral weight under the universal interband background is $e^2\pi/(8h)4mv_F^2$. In contrast to the known result for graphene no strict conservation law applies to the spectral weight transfers between inter and intra band transition brought about by variations in the magnitude of the chemical potential when a non-relativistic contribution is present in the Hamiltonian whatever size it may have.

PACS numbers: 78.20.Ls, 71.70.Di, 73.25.+i

I. INTRODUCTION

Since the initial theoretical discussion and experimental discovery of topological insulators,¹⁻⁴ their topologically protected metallic surface states have been extensively studied, both because of the new physics involved and because of novel functionality that could find application in a next generation of electronic devices. Another class of materials which is also of great importance for possible device applications are those used in studies of spintronics.⁵⁻⁹ Both classes involve the spin orbit interaction. For topological insulators this interaction is strong and the linear in momentum relativistic (Dirac) part of the single particle Hamiltonian proportional to the Fermi velocity (v_F) dominates over a smaller non-relativistic (Schrödinger) quadratic in momentum piece characterized by a mass (m). By contrast, in the materials of interest for spintronics, the Schrödinger contribution dominates over the weak Dirac contribution. In a first approximation, the same minimal model Hamiltonian can be used to describe both cases, but the magnitude of the parameters involved in the Dirac and Schrödinger contribution are very different.

In presently studied materials, the Schrödinger mass can vary from the order of the bare electron mass (m_e) to one tenth its value and even less. While the Fermi velocity v_F is of order 5×10^5 m/s in topological insulators, in spintronic materials it is less than a few times 10^3 m/s and often much smaller.⁵ This large difference in the magnitude of the spin orbit coupling between these two classes of materials can lead to profound differences in their physical properties. For example in topological insulators the DC quantum Hall effect shows a quanti-

zation $n = 1/2, 3/2, 5/2, \dots$ while in semiconductors it is $n = 0, 1, 2, 3, \dots$ ¹⁰⁻¹⁶

The AC magneto response of materials has been widely studied and provides valuable information on electron dynamics. Recent related studies include graphene,¹⁷⁻²³ silicene,^{24,25} topological insulators,²⁶⁻²⁸ MoS_2 ²⁹ and Weyl semimetals.³⁰ In topological insulators one is dealing with real electron spin and spin momentum locking has been observed.³¹⁻³⁴ For graphene and other two dimensional membranes such as silicene which displays buckling and planar MoS_2 , it is the pseudo spin associated with the two sublattices of the honeycomb lattice which is involved. Weyl or Dirac semimetals are a three dimensional version of graphene. There have also been studies of Kerr and Faraday effects in thin films with the breaking of time-reversal symmetry^{35,36}. Magneto transport studies^{37,38} with emphasis on the transition between ordinary and topological insulator states described by a massive Dirac fermion model with change in sign of the mass term. Studies are also available on magneto-optics of bilayer³⁹, multilayer⁴⁰ graphene and graphene on polar substrates⁴¹. Finally we mention magneto-phonon resonances in graphene studied by Raman spectroscopy⁴².

In this paper we study the magneto-optical response of a two dimensional electron gas with Hamiltonian (H) consisting of a combination of relativistic and non-relativistic piece. We feature prominently the effect of a small spin orbit coupling when the non-relativistic part of H is dominant. We also compare with results, some known but many new, that apply in the opposite limit of a topological insulator for which the spin orbit coupling dominates. Both dynamic AC transverse ($\sigma_{xy}(\omega)$)

and longitudinal ($\sigma_{xx}(\omega)$) conductivity are considered. In section II we provide the formal expressions for the magneto-optical conductivity based on our chosen Hamiltonian. We also give simplified but approximate formulas for the optical spectral weight of the various absorption lines which correspond to the underlying Landau level (LL) structure created by the magnetic field in the limit where the Schrödinger part is dominant. We work to leading order of Dirac (E_1) to Schrödinger (E_0) magnetic energy scale assuming their ratio to be small. We explicitly consider the case when the chemical potential μ is much larger than E_0 . In section III we provide numerical results for both $\text{Re}\sigma_{xx}(\omega)$ and $\text{Im}\sigma_{xy}(\omega)$ when E_1 is increased and is no longer much smaller than E_0 . Particular attention is paid to the emergence of the interband background associated with optical transition between the split helical bands caused by the spin-orbit coupling. This background is found to be of constant magnitude independent of the size of v_F but is non-zero only in a very limited photon window. We also present results when the magnetic field is zero. These greatly help in the physical understanding of the finite B case. Readjustments of optical spectral weight due to variations in chemical potential are described. In section IV we turn to the limit when it is the Dirac energy which dominates. We provide simplified but analytic expressions which show the first non-zero corrections to the pure relativistic case for the optical spectral weight when a small subdominant Schrödinger contribution is also included i.e. $E_0/E_1 \ll 1$. Numerical results are provided when our simplified expression is no longer valid and comparison with the limit $E_1/E_0 \ll 1$ is made. In section V we give more details on spectral weight redistribution with variations in chemical potential μ . A summary and conclusions are found in section VI.

II. FORMALISM

The Hamiltonian on which this work is based takes on the form

$$H_0 = \frac{\hbar^2 k^2}{2m} + \hbar v_F (k_x \sigma_y - k_y \sigma_x) \quad (1)$$

where \mathbf{k} is momentum, m is the Schrödinger mass, v_F the Dirac Fermi velocity and σ_x, σ_y spin Pauli matrices. For spintronic materials the first term in (1) is dominant with the second small in comparison; while for topological insulator it is the opposite. This is shown schematically in Fig.1. The dashed black curve (left frame) is the perfect cone which would apply for example to the Dirac fermions of graphene and is included here for comparison with the heavy solid red curve which illustrates the dispersion curve found in topological insulators. In this case the subdominant Schrödinger piece in the Hamiltonian (1) reshapes the cone into an hourglass figure with upper conductance band (red) narrowing in cross-section as compared with the Dirac cone and lower valence band

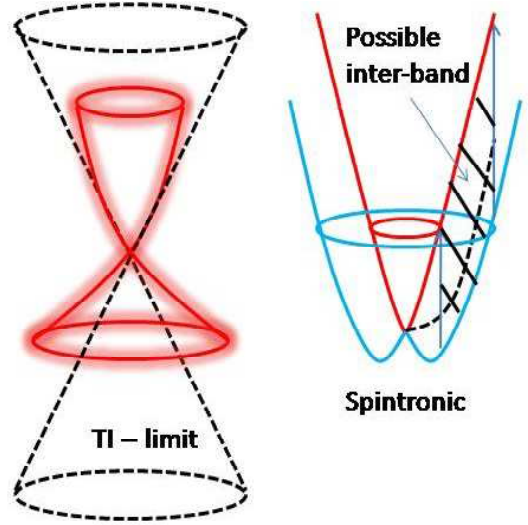


FIG. 1. (Color online) Schematics of dispersion curves used to describe a topological insulator (left hand figure) and the opposite limit of weak spin orbit coupling (right hand figure).

(red) fanning out from the cone giving it a larger cross-section. The right hand frame illustrates the other limit of dominant Schrödinger quadratic band (black dashed curve) with subdominant spin orbit coupling. This leads to a splitting of the dashed curve into two bands with heavy solid red (E_+) contained inside the solid blue (E_-) dispersion curve.

When a magnetic field B is applied perpendicular to the plane of the two dimensional Hamiltonian (1), Landau levels (LL) form and the dynamic magneto-conductivity is given by²⁶

$$\sigma_{\alpha\beta}(\omega) = \frac{-i}{2\pi l_B^2} \sum_{N,N',s,s'} \frac{f_{N,s} - f_{N',s'}}{E_{N,s} - E_{N',s'}} \times \frac{\langle N, s | j_\alpha | N', s' \rangle \langle N', s' | j_\beta | N, s \rangle}{\omega - E_{N,s} + E_{N',s'} + i/(2\tau)} \quad (2)$$

where we have included a small phenomenological constant residual broadening of $1/(2\tau)$. In Eq. (2) $l_B = 1/\sqrt{e|B|/\hbar}$ is the magnetic length with e the electron charge, f the Fermi distribution, $E_{N,s}$ the Landau level energies with eigenfunction $|N, s\rangle$. The matrix elements $\langle N, s | j_\alpha | N', s' \rangle$ with j_α the α' th component of the current operator carry the information on the optical selection rules. The Fermi function $f_{N,s} \equiv 1/[e^{\beta(E_{N,s}-\mu)} + 1]$ with β the inverse temperature and μ the chemical potential. Details can be found in reference (26) with their Eq. (10) corrected to include an overall additional minus sign in the second line. The eigen energies are given by

$$E_{N,s} = NE_0 + s\sqrt{(E_0/2)^2 + 2NE_1^2} \quad (3)$$

for $N = 1, 2, 3, \dots$, $s = \pm$ and

$$E_{N=0} = E_0/2. \quad (4)$$

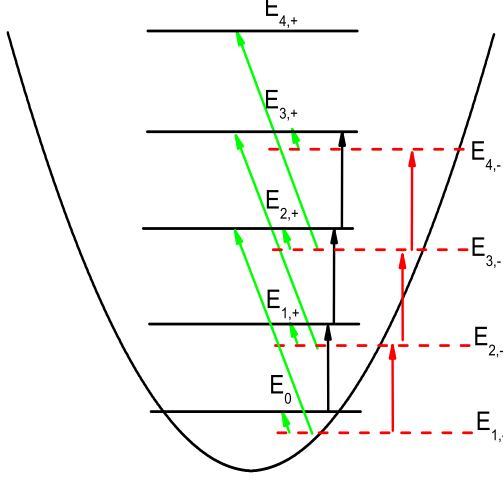


FIG. 2. (Color online) Schematic of possible optical transitions in the limit of small spin orbit coupling. The intraband transitions (+ + solid black arrows) and (− − solid red arrows) have optical spectral weight of order one and remain finite when $v_F = 0$. The interband transitions (solid green arrows) have weight of order P^2 for (+ −) and P^3 for (− +).

Here $E_1 = \hbar v_F \sqrt{e|B|/\hbar}$ is the Dirac magnetic energy scale and $E_0 = \hbar^2/(m l_B^2)$ is the corresponding Schrödinger magnetic energy scale. We begin with the limit when, for a given value of the magnetic field B , $E_1 < E_0$. Reference (26) was exclusively concerned with the opposite limit $E_1 > E_0$ which applies to topological insulators. When appropriate we provide comparisons between these two cases. In a later section we also present additional new results in the TI limit as well. When $E_1 \rightarrow 0$, the energies $E_{N,s} \simeq (N + s/2)E_0 + \frac{sE_0}{2}8NP$ with $P \equiv (E_1/E_0)^2$ for $N = 1, 2, 3, \dots$ and $E_{N=0} = E_0/2$. Clearly in this case we are dealing with two separate Schrödinger Landau level series with the $N = 0$ term included with $E_{N,+}$ ($N \geq 1$). These two series can be thought of as originating from the spin degeneracy of a simple quadratic band split by a small spin-orbit coupling term which shifts one band up and the other down in energy. This is illustrated in Fig. 2 where we show the $E_{N,-}$ series as red dashed horizontal lines and the E_0 plus $E_{N,+}$ as solid black horizontal lines.

The final form of the equations for the absorptive part of the dynamic conductivity $\text{Re}\sigma_{xx}(\omega)$ and $\text{Im}\sigma_{xy}(\omega)$ respectively for longitudinal and Hall conductivity given in Eq. (22) of reference (26) will be our starting point.

They are

$$\begin{aligned} & \mp \frac{e^2}{2\hbar} \sum_s (f_0 - f_{1,s}) \frac{F(0, s)}{H(0, s)} E_0 \\ & \times [\delta(\hbar\omega - E_0 H(0, s)) \pm \delta(\hbar\omega + E_0 H(0, s))] \\ & \mp \frac{e^2}{2\hbar} \sum_{N=1, s, s'} (f_{N,s} - f_{N+1, s'}) \frac{F(N, s, s')}{H(N, s, s')} E_0 \\ & \times [\delta(\hbar\omega - E_0 H(N, s, s')) \\ & \pm \delta(\hbar\omega + E_0 H(N, s, s'))] \end{aligned} \quad (5)$$

where the upper sign applies to $\text{Re}\sigma_{xx}(\omega)$ and the lower sign to $\text{Im}\sigma_{xy}(\omega)$. It is clear from the form of equation (5) that the optical matrix elements have restricted the possible transitions between LL to $N, s \rightarrow N + 1, s'$ with $F(N, s, s') = \langle N, s | j_\alpha | N', s' \rangle \langle N', s' | j_\beta | N, s \rangle \pi$ and $H(N, s, s') = -1 + s\sqrt{1/4 + 2NP} - s'\sqrt{1/4 + 2(N+1)P}$ related to the energies of the possible optical transitions. While the complicated expressions for $F(N, s, s')$ specified in reference (26) (not repeated here as they are rather complicated and not particularly illuminating) are to be used in the numerical results that we will present later, it is helpful to start with approximate expressions which apply in the limit of small P . Defining $\mathcal{F}(N, s, s') \equiv F(N, s, s')E_0/H(N, s, s')$ we find for the intraband optical transitions to leading order ($N = 1, 2, \dots$) and for $N = 0$ ¹⁶

$$\mathcal{F}(N, -, -) = -N/2(1 - 4NP^2)E_0 \quad (6)$$

$$\mathcal{F}(N, +, +) = -(1 + N)/2[1 + 4(N + 1)P^2]E_0 \quad (7)$$

with next corrections higher order in P and for the interband transition

$$\mathcal{F}(N, +, -) = 2(1 + 2N)P^2E_0 \quad (8)$$

$$\mathcal{F}(N, -, +) = -8N(1 + N)P^3E_0 \quad (9)$$

The first thing that needs to be emphasized is that the interband transition carry little optical spectral weight in the limit $P \ll 1$. The (+, −) transitions go like the square of P and correspond to the absorption of photon that have small energies as seen in Fig. 2 (short green arrows). Such transition vanish as $P \rightarrow 0$. The (−, +) optical transitions (long green arrows) go like the cube of P and so are even less important. These correspond to finite photon energies with limiting value of $2E_0$ as $P \rightarrow 0$ as seen in Fig. 2. In contrast the intraband transitions remain finite as $P \rightarrow 0$ and so dominate the optical absorption. They represent the only possible absorption processes in a pure non relativistic system with no spin-orbit coupling. This is clear from Fig. 2 where the black arrows indicate the (+, +) intraband and red arrows the (−, −) intraband transitions. For a typical spintronic material at an applied magnetic field B of one tesla, $E_0 \simeq 1.16$ meV for $m = 0.1m_e$ (with m_e

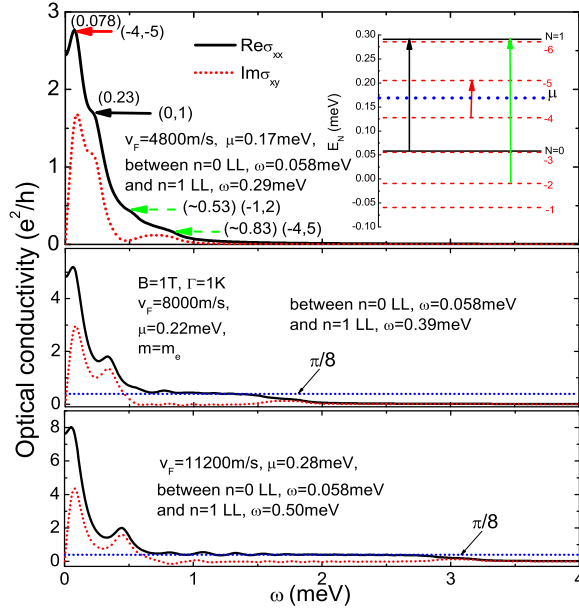


FIG. 3. (Color online) The dynamic longitudinal $\sigma_{xx}(\omega)$ (solid black curve) and transverse $\sigma_{xy}(\omega)$ (Hall, dotted red curve) conductivity in units of e^2/h as a function of photon energy $\hbar\omega$ in meV. In all cases the Schrödinger mass m was set at its free electron value m_e , the magnetic field at $B = 1$ Tesla, the broadening $\Gamma = 1K$ and the chemical potential μ is half way between the $N = 0$ and $N = 1$ Landau level (LL). The Schrödinger magnetic energy scale $E_0 = 0.116$ meV while the Dirac scale E_1 is varied and is 0.116 meV for $P = 1$ in the top frame, 0.194 meV for $P = 2.8$ in the middle frame and 0.272 meV for $P = 5.5$ in the bottom frame. The corresponding Dirac Fermi velocities are 4.8×10^3 m/s, 8×10^3 m/s and 11.2×10^3 m/s respectively. In the top frame arrows highlight the energies of some of the allowed optical transitions which contribute to the dynamic conductivity. The relevant LL energy scheme is given in the inset where the chemical potential is shown as the horizontal dotted blue line.

the bare electron mass) and for a Dirac Fermi velocity $v_F \simeq 4.3 \times 10^3$ m/s, $E_1 \simeq 0.104$ meV which corresponds to a P value of $\simeq 0.008$. Even if the magnetic field is reduced by a factor of fifty our expansion parameter $P \simeq 0.4$ and consequently the interband optical transitions are suppressed by a factor of $(0.4)^2 = 0.16$ which is still small. It is important however to realize in this context that our expansion in small P implies that we are working at finite value of magnetic field (here 1 Tesla for definiteness). Because E_1 goes like \sqrt{B} and E_0 goes instead like B , at very low field the Dirac energy scale will always be larger than the Schrödinger magnetic energy scale and we are mapped out of the small P regime.

III. NUMERICAL RESULTS

In Fig. 3 we show results of complete numerical calculations based on Eq. (5) without making the approx-

imation that P be very small and using the exact expressions for the optical matrix elements in $F(N, s, s')$.²⁶ In the top frame we show $Re\sigma_{xx}(\omega)$ (solid black curve) and $Im\sigma_{xy}(\omega)$ (dotted red curve) in units of e^2/h as a function of photon energy ω in meV. Here $E_0 = E_1 = 0.116$ meV, $v_F = 4.8 \times 10^3$ m/s with chemical potential μ set half way between the $N = 0$ and $N = 1$ LL ($\mu = 0.17$ meV). We have also used a residual scattering $\Gamma = 1/2\tau = 1K$ which broadens out the LL although structures corresponding to the allowed optical transitions between levels are still seen and some of these are identified by arrows. Black and red are intraband, green interband in both main frame and on energy level inset. The inset gives the details of the allowed optical transitions including the position of the chemical potential at $.17$ meV (dotted blue horizontal line). We first note that E_{N-} is negative only for $N = 1$ and 2 and is near the level with $N = 0$ for $N = 3$. It becomes larger than the value of the chemical potential for $N = 5$ which means that this level is unoccupied and hence the interband transition are limited to 7 with the $-4 \rightarrow 5$ corresponding to a photon energy of $.82$ meV which is seen as a cut off for both longitudinal and transverse optical conductivity as indicated by a green arrow. The lowest energy transition is intraband at 0.078 meV and the second intraband is at 0.23 shown by the red and black arrows in the inset. Only 9 transitions are possible, two intraband and seven interband, one shown as the green arrow in the level scheme diagram. This is in sharp contrast to the pure Dirac case for which the interband transitions have no natural cut off in our continuum limit Hamiltonian (1). Note that the magnetic energy scale is small and that, even for $\Gamma = 1K$ which is certainly reasonable, the broadening has eliminated the sharp peaks at the LL energies. Finally we note that, by choice, P was set to be 1 so that we are far away from the $P \ll 1$ limit considered in the simplified Eq. (6) to (9). Nevertheless, the interband transition still correspond to suppressed optical spectral weight. In the second frame of Fig. 3 we have increased the value of P to 2.8 and $\mu = 0.22$ meV which is again half way between $N = 0$ and $N = 1$ Landau level. Now we see the emerging of a prominent and distinct interband background in $Re\sigma_{xx}(\omega)$ on which is superimposed very broadened LL peaks. This background extends to almost $\lesssim 2.0$ meV and its height in units of e^2/h is exactly $\pi/8$ (shown as the dotted blue line). Remarkably this is precisely the value found in graphene except for the factor of 4 which accounts for valley and spin degeneracy. The interband background is even more prominently developed in the lower frame of Fig. 3 for $P = 5.5$. Here the cutoff is $\lesssim 3.0$ meV.

We can gain insight into these results by comparing with results obtained in the topological insulator limit as we will do in the next section. Before we do this however it is also useful to consider the limit of zero magnetic

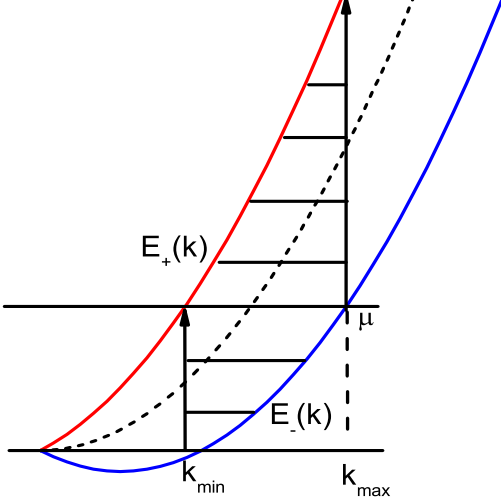


FIG. 4. (Color online) The pure Schrödinger quadratic in k dispersion curve (dashed line) compared with $E_+(k)$ (solid red) and $E_-(k)$ (solid blue) dispersion. The vertical arrows show the two extremum interband transitions that are possible from which we identify k_{\min} and k_{\max} . The shaded region emphasizes the area associated with such allowed transitions.

field. In that case the formula for $Re\sigma_{xx}(\omega)$ is given by

$$\frac{e^2}{\omega} \frac{1}{4\pi^2} \int_0^\infty [f(E_-(k)) - f(E_+(k))] k dk$$

$$(\hbar v_F)^2 \int_0^{2\pi} d\theta \pi \delta(\hbar\omega - E_+(k) + E_-(k)) \quad (10)$$

with

$$E_s(k) = \frac{\hbar^2 k^2}{2m} + s\hbar v_F k \quad (11)$$

The first thing to note about Eq. (10) is that the Schrödinger contribution to the energy drops out of the interband energy difference $[E_+(k) - E_-(k)]$ but it does remain in the thermal factor $[f(E_-(k)) - f(E_+(k))]$. At zero temperature this factor reduces either to one in the interval for which interband transitions are possible or is otherwise zero. The kinematics involved are shown in Fig. 4. The red solid line gives $E_+(k)$ vs k , the blue is $E_-(k)$ and the black dashed curve, which is for comparison, gives the dispersion curve when the spin-orbit term is zero i.e. $v_F = 0$ in Eq. (11). The shaded region shows the possible interband transitions and defines a minimum and a maximum value of momentum k_{\min} and k_{\max} , which provide lower and upper limits on the integral in Eq. (10). These cut offs are due to the thermal factors which require an occupied initial state and an unoccupied final state. For graphene k_{\min} corresponds to the onset of interband absorption at a photon energy of exactly twice chemical potential 2μ . In that case however k_{\max} does not exist, since $E_-(k)$ is negative for all values

of k and never crosses the chemical potential ($\mu > 0$). Applying these restriction to Eq. (11) means that interband optical transitions are only possible for energies between

$$\omega_{\min} = E_+(k_{\min}) - E_-(k_{\min}) \quad (12)$$

and

$$\omega_{\max} = E_+(k_{\max}) - E_-(k_{\max}). \quad (13)$$

But the application of these cut off on momentum in Eq. (10) is the only effect of the thermal factors which, at zero temperature, have magnitude of one. This means that the remaining integral is identical to that for graphene leading to precisely the same absolute value of the universal background. Of course now the background is restricted to the interval ω_{\min} to ω_{\max} . Thus $Re\sigma_{xx}(\omega)$ for interband absorption is still equal to $e^2\pi/8h$ but is non zero only for photon energies $\omega_{\min} \leq \omega \leq \omega_{\max}$. This remarkable result is consistent with the general trends found in our numerical work presented in Fig. 3 for the case of a finite B . Simple formulas for ω_{\min} and ω_{\max} are easily obtained

$$\omega_{\min} = -2mv_F^2 + 2\hbar v_F \sqrt{\left(\frac{mv_F}{\hbar}\right)^2 + \frac{2m\mu}{\hbar^2}} \quad (14)$$

$$\omega_{\max} = 2mv_F^2 + 2\hbar v_F \sqrt{\left(\frac{mv_F}{\hbar}\right)^2 + \frac{2m\mu}{\hbar^2}} \quad (15)$$

We can check that in the limit $m \rightarrow \infty$ (pure relativistic case) $\omega_{\max} = \infty$ and $\omega_{\min} = 2\mu$. In the opposite limit of $v_F \rightarrow 0$ both ω_{\min} and ω_{\max} are zero and there are no interband transitions. In all cases the width of the photon window over which the universal background has height $e^2\pi/8h$ is $\omega_{\max} - \omega_{\min} = 4mv_F^2$ which is linear in m and quadratic in v_F , and is independent of the chemical potential μ . However, both the onset and termination of the interband background do depend on the chemical potential μ which appears in the square root factor of Eq. (14) and this shifts both upper and lower limits on the interband absorption. A similar effect holds when a magnetic field is additionally applied, as we will describe below. First we note that the total optical spectral weight (W_{IB}) in the interband background is $W_{IB} = (e^2\pi/8h \times 4mv_F^2)$. In addition there are the intraband transitions which give the Drude response. In the appendix we show that the optical spectral weight contained in the Drude when $B = 0$ is given by

$$\frac{e^2 m (\sqrt{\hbar^2 v_F^2 + (2\hbar^2/m)\mu} - \hbar v_F) \sqrt{\hbar^2 v_F^2 + (2\hbar^2/m)\mu}}{8\hbar^3} +$$

$$\frac{e^2 m (\sqrt{\hbar^2 v_F^2 + (2\hbar^2/m)\mu} + \hbar v_F) \sqrt{\hbar^2 v_F^2 + (2\hbar^2/m)\mu}}{8\hbar^3} \quad (16)$$

where the first line comes from the $(+, +)$ transitions and the second from the $(-, -)$ transitions. Formula (16) applies also to the opposite limit of a topological insulator

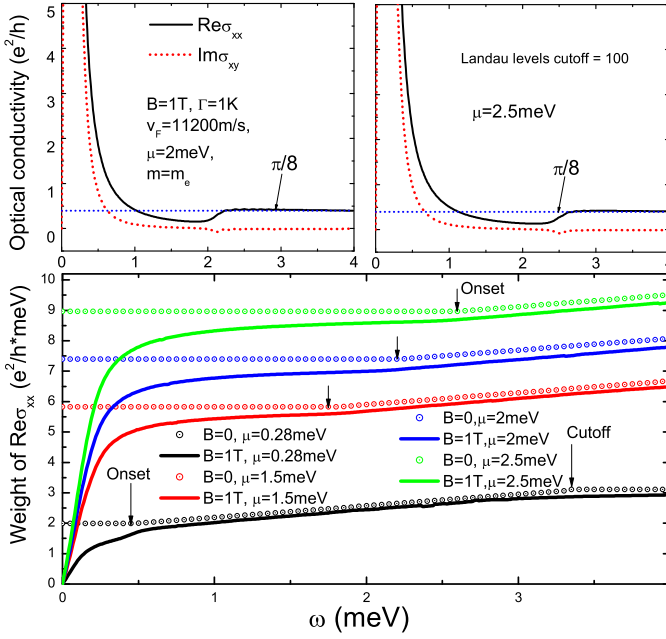


FIG. 5. (Color online) Top frame, the dynamic longitudinal $\sigma_{xx}(\omega)$ (solid black curve) and transverse $\sigma_{xy}(\omega)$ (Hall, dotted red curve) conductivity in units of e^2/h as a function of photon energy $\hbar\omega$ in meV. Parameters are the same as for the bottom frame of Fig.3 except that different values of chemical potential are employed namely $\mu = 2.0$ meV and $\mu = 2.5$ meV. Bottom frame, the optical sum $W(\omega_c)$ as a function of upper cut off ω_c of the longitudinal conductivity $\sigma_{xx}(\omega)$. The four curves are for $\mu = 0.28$ meV (black), $\mu = 1.5$ meV (red), $\mu = 2.0$ meV (blue) and $\mu = 2.5$ meV (green). The dotted curves are for the case of $B = 0$ and are included for comparison with the solid curves for $B = 1$ Tesla.

but in this case only the first line is retained since only the $(+, +)$ transitions are possible. For the non-relativistic limit the Drude weight W_D is

$$W_D = \frac{e^2\pi}{h}[\mu + \frac{1}{2}mv_F^2]. \quad (17)$$

Thus W_D does depend on the chemical potential μ in contrast to the interband contribution W_{IB} . The total optical spectral weight $W_T = W_D + W_{IB} = \frac{e^2\pi}{h}[\mu + mv_F^2]$. We will return to this fact later when we consider spectral weight redistribution between intra- and inter-band transition as μ is varied and compare with the case of topological insulators. In the top frame of Fig. 5 we show results for the real part of the longitudinal dynamic conductivity ($Re\sigma_{xx}(\omega)$, solid black curve) and the imaginary part of the transverse Hall conductivity ($Im\sigma_{xy}(\omega)$, dotted red curve) for the same parameters as in the bottom frame of Fig. 3 but now the chemical potential has been increased. In the left frame $\mu = 2.0$ meV and in the right frame $\mu = 2.5$ meV. Increasing μ eliminates several interband transitions which now are no longer possible because of Pauli blocking. The optical spectral weight of these interband transitions has been transferred partly

to the low energies intraband peak which becomes more prominent with increasing μ . In the lower frame of Fig. 3 a background of height $\frac{e^2\pi}{8h}$ is well defined in the longitudinal conductivity down to photon energies $\lesssim 1$ meV. On the other hand in the top frame of Fig. 5 this background is very suppressed in the region 1 meV to $\sim \mu$ where it is seen to jump to its universal value. For the case of $B = 0$ we saw that this threshold energy is ω_{min} , defined in Eq. (14). This universal background then remains up to an upper cut off ω_{max} defined in Eq. (15) for $B = 0$ at which point it drops to zero. For finite B these critical energies are somewhat different from those of Eq. (14) and vary with the magnitude of B . In Fig. 5 (top frame) $B = 1$ Tesla. Increasing B increases the distance in energy between the various Landau levels and so the energy of the minimum and maximum possible interband transition is changed.

A more quantitative look at spectral weight distribution between inter and intra band optical transition and its variation with value of the chemical potential μ is given in the lower frame of Fig. 5. There we present results for the total spectral weight contained in the longitudinal conductivity below a variable upper photon energy ω defined as

$$W(\omega) = \int_0^\omega Re\sigma_{xx}(\omega')d\omega' \quad (18)$$

The units on $W(\omega)$ are $\frac{e^2}{h}$ times meV's and ω on the horizontal axis is in meV. Four values of chemical potential μ are shown $\mu = 0.28$ meV (black), $\mu = 1.5$ meV (red) $\mu = 2.0$ meV (blue) and $\mu = 2.5$ meV (green). Here the residual scattering rate $\Gamma = 1K$, the Fermi velocity $v_F = 11200$ m/s and the Schrödinger mass m is equal to the bare electron mass (m_e).

The solid curves are for a magnetic field of $B = 1$ Tesla while the color coded open circles which are shown for comparison, are for zero magnetic field. For the first black curve with small value of chemical potential μ , inter and intra band contributions to $Re\sigma_{xx}(\omega)$ and to its integrated spectral weight $W(\omega)$ are not easily distinguished although there is a clear onset, slightly below $\omega = 0.5$ meV, indicated by the black arrow, and there is also a cut off energy around 3.4 meV (see black arrow) beyond which the integrated spectral weight $W(\omega)$ ceases to increase. This is seen particularly clearly in the curve for $B = 0$. For the other three cases considered, the intra and interband transitions are well separated. Below the onset of the interband transition at ω_{min} of Eq. (14), the $B = 0$ curve is completely flat and contains the Drude spectral weight W_D of formula (17). At $\omega = \omega_{min}$ there is an abrupt change in slope from zero to a finite amount set by the value of the universal background $\frac{e^2\pi}{8h}$. This kink, which we marked with a black arrow, while most pronounced in our $B = 0$ curves is also present at a slightly different energy in our $B = 1$ Tesla curves. This is expected and is traced to our numerical results for the absorptive part of the longitudinal conductivity

shown in the top frame of Fig. 5 where the onset of the universal interband background is clearly seen around $\omega = \omega_{min}$. The intraband transitions below this onset provide a peak in $Re\sigma_{xx}(\omega)$, displayed from $\omega = 0$, which has however decayed to very small values before $\omega = \omega_{min}$ is reached. It is the displacement of the intraband transition (which provides a Drude when $B=0$) to finite frequency in a nonzero magnetic field ($B=1$) which accounts for the gradual increase in $W(\omega)$ out of zero energy ($\omega = 0$) towards the Drude plateau of the $B=0$ case which is now never perfectly flat.

Beyond the region of linear increase in $W(\omega)$, in our $B=0$ case the optical spectral weight reaches saturation as can be seen in the black curves for which ω_{max} of Eq. (15) falls within the range of energies shown in the figure. For the other cases one needs to go to energies beyond 4 meV. The saturated value for $B=0$ is the sum of the Drude contribution of Eq. (17) plus the amount in the interband which add up to $\frac{e^2\pi}{h}[\mu + mv_F^2]$.

This behavior is very different from what is known for the pure relativistic case such as for graphene for which no upper cutoff exists other than the Brillouin zone cut off. While we will see in a later section that modifications of the known graphene behavior also arise when a small subdominant Schrödinger piece is added to the dominant Dirac contribution, for the pure relativistic case spectral weight is simply redistributed between inter and intra contributions as μ is varied. Here we see that for materials with both Dirac and Schrödinger pieces in the Hamiltonian there is no strict conservation of spectral weight with changes in μ , an issue we will return to in section V. While only μ changes in the various curves shown in the lower frame of Fig. 5, they do not merge as ω gets large.

IV. COMPARISON WITH A TOPOLOGICAL INSULATOR

We next compare the results of Fig. 3 with results obtained in the topological insulator limit shown in Fig. 6. The three top frames give the absorptive part of the diagonal conductivity $Re\sigma_{xx}(\omega)$ (solid black curve) and comparison with the imaginary part of transverse conductivity $Im\sigma_{xy}(\omega)$ (dotted red curve) in units of e^2/h as a function of photon energy ω in meV. We have taken the Fermi velocity to be 4.3×10^5 m/s, the magnetic field to be 1 Tesla, the scattering rate $\Gamma = 15K$ and the Schrödinger mass equal to the bare electron mass (m_e) in the third lowest frame, $m = 0.1m_e$ in the second lowest frame and $m = 0.05m_e$ in the top frame. Decreasing m moves us further away from the pure Dirac case which would correspond to graphene. In all these frames the chemical potential was set to fall halfway between $N = 1$ and $N = 2$ Landau level. The first thing to note about these results is that the magnetic energy scale associated with the Landau levels is much larger than that in Fig. 3 for the non-relativistic limit. Here the relativistic energy

scale given by the Dirac term only is $E_1 = 10.4meV$ while the non relativity magnetic energy scale for $m = m_e$ is 0.116 meV, two orders of magnitude smaller. Secondly the interband optical peaks in $Re\sigma_{xx}(\omega)$ remain to very high energies as in the case of graphene previously discussed in Ref. (17). Just as we found it enlightening in Fig. 3 to consider several values of v_F for fixed value of m , here we fix v_F and consider 3 values of m . For $m = m_e$ third frame from top in Fig. 6 the results are not significantly different from those in pure graphene. As m is decreased to $0.1m_e$ a splitting of the peaks in $Re\sigma_{xx}(\omega)$ into pairs is seen. This arises because the Schrödinger term breaks the particle hole symmetry of the pure relativistic case and the optical transition $-N$ to $N + 1$ no longer has the same energy as $-(N + 1)$ to N . This splitting is even more pronounced when m is decreased further to $m = 0.05m_e$ as in the top frame. In this case not all peaks can be easily identified as split pairs. Of course even for $m = m_e$, (third frame down) there should in principle be a splitting but here we have taken a smearing parameter $\Gamma = 15K$ which is enough to merge them so that a single peak is effectively seen.

We will return to the results of Fig. 6 later. First it is useful to consider analytic results which we can obtain only in the limit of $P^{-1} \ll 1$ when the non relativistic correction to pure Dirac is small. In this case the optical spectral weight in units of $e^2/2h$ which is associated with the allowed transitions at zero temperature have the approximate form^{16,26}

$$\mathcal{F}(N, -, -) = \left[\frac{\sqrt{N} + \sqrt{N+1}}{4\sqrt{2}} - \frac{1/\sqrt{P}}{16[\sqrt{N(1+N)} - 2\frac{N(N+1)}{1+2N}]} \right] E_1 \quad (19)$$

which will not be needed for $\mu \geq 0$ because such transitions are Pauli blocked

$$\mathcal{F}(N, +, +) = -\left[\frac{1}{4\sqrt{2}[-\sqrt{N} + \sqrt{N+1}]} + \frac{1/\sqrt{P}}{16[\sqrt{N(1+N)} - 2\frac{N(N+1)}{1+2N}]} \right] E_1 \quad (20)$$

$$\mathcal{F}(N, -, +) = \left[\frac{-1}{4\sqrt{2}[\sqrt{N} + \sqrt{N+1}]} + \frac{1/\sqrt{P}}{16[\sqrt{N(1+N)} + 2\frac{N(N+1)}{1+2N}]} \right] E_1 \quad (21)$$

and

$$\mathcal{F}(N, +, -) = \left[\frac{1}{4\sqrt{2}[\sqrt{N} + \sqrt{N+1}]} + \frac{1/\sqrt{P}}{16[\sqrt{N(1+N)} + 2\frac{N(N+1)}{1+2N}]} \right] E_1 \quad (22)$$

where we are working to lowest order in $1/\sqrt{P}$. This provides the first correction to the pure relativistic limit. Note that, in addition to the $\mathcal{F}(N, s, s')$, the absorptive part of the longitudinal optical conductivity $\text{Re}\sigma_{xx}(\omega')$ depends additionally on thermal factors which give a $+1$ or -1 at $T = 0$. consequently the optical spectral weight under an allowed optical transition between LL which must be positive, is in all cases equal to the absolute value of $\mathcal{F}(N, s, s')$. This means that the spectral weight corresponding to (20) and (21) carries an additional minus sign so that the optical spectral weight associated with (21) is reduced over its pure Dirac limit value while that associated with (22) is increased by exactly the same amount. When this correction is dropped, we recover the result of Gusynin, Sharapov and Carbotte¹⁷ for graphene except for a missing factor of four accounting for spin and valley degeneracy not present for topological insulators. Taking the limit of large N the optical spectral weight contained in the intraband transitions is given by $\frac{e^2}{2\hbar}\mathcal{F}(N, +, +)_{N \rightarrow \text{large}}$. Noting that $\frac{1}{[-\sqrt{N} + \sqrt{N+1}]} \simeq 2\sqrt{N}$ and that $\frac{1}{[\sqrt{N(1+N)} - 2\frac{N(N+1)}{1+2N}]} \simeq 2N$ we get

$$-\frac{e^2}{2\hbar}\mathcal{F}(N, +, +)_{N \rightarrow \text{large}} = \left[\frac{\sqrt{2N}}{4} + 1/\sqrt{P}\frac{N}{2}\right]E_1 \quad (23)$$

But $\mu \simeq \sqrt{2N}E_1 + E_0(\frac{\mu}{E_1\sqrt{2}})^2$ or $\sqrt{2N} \simeq \frac{\mu}{E_1}(1 - \frac{\mu}{2mv_F^2})$ so that

$$-\frac{e^2}{2\hbar}\mathcal{F}(N, +, +)_{N \rightarrow \text{large}} \simeq \frac{\mu}{4}\left(1 + \frac{\mu}{2mv_F^2}\right)\frac{e^2\pi}{h} \quad (24)$$

In the limit of $m = \infty$ this reduces to $\frac{e^2\pi}{4h}\mu$ which is exactly the amount of optical spectral weight there would be under the Drude in the $B = 0$ limit in graphene except for the factor of 4 in the denominator which would be canceled by a degeneracy factor for two spins and two valleys. When m is large but not infinite the spectral weight under the intraband transition line is increased from a normalized value of 1 by an amount $\frac{\mu}{2mv_F^2}$. For our expansion to be valid we still need $\frac{\mu}{4mv_F^2}$ to be small which is a more restrictive condition than simply $1/\sqrt{P} \ll 1$. Nevertheless it shows clearly that the optical spectral weight residing in the various optical lines is changed from the pure Dirac case when a subdominant Schrödinger piece is also present in the Hamiltonian.

In the large N limit the intraband line is the cyclotron resonance line of semiclassical theory. The cyclotron frequency was worked out in Ref. [26] and found to be to lowest order correction for a small Schrödinger contribution,

$$\hbar\omega_c = \frac{E_1^2}{\mu}\left[1 + \frac{3}{2}\mu/(mv_F^2)\right] \quad (25)$$

So that $\hbar\omega_c$ is increased for $m \neq \infty$ as is the spectral weight under this line. It is interesting to compare the

spectral weight of the cyclotron resonance line with the Drude weight (W_D) for the zero magnetic field case. The expression for W_D is (Eq. (16), first line only)

$$\frac{e^2m[\hbar^2v_F^2 + (2\hbar^2/m)\mu - \hbar v_F\sqrt{\hbar^2v_F^2 + (2\hbar^2/m)\mu}]}{8\hbar^3} \quad (26)$$

which is valid for any value of m . Assuming m to be large but not infinite we can expand (26) and obtain a first correction to pure Dirac, we get

$$W_D = \frac{e^2\pi}{4h}\mu\left[1 + \frac{\mu}{2mv_F^2}\right] \quad (27)$$

which agrees perfectly with the spectral weight under the semiclassical cyclotron line in this approximation.

In the comparisons made so far between the pure Dirac case and a topological insulator with finite Schrödinger contribution we have considered the chemical potential as fixed. It is important to realize that this does not correspond to a fix doping as m is varied. For a fix density of charge carriers(n) away from the neutrality point we have that

$$n = \int_0^{k_{\min}} \frac{kdk}{2\pi} = \frac{1}{4\pi}\left[\frac{-mv_F}{\hbar} + \frac{mv_F}{\hbar}\sqrt{1 + \frac{2\mu}{mv_F^2}}\right]^2 \quad (28)$$

where we have used k_{\min} determined from Fig. 4. Eq. (28) holds whatever may be the value of m . For large m retaining the first leading correction we get

$$n \simeq \frac{1}{4\pi}\left(\frac{\mu}{\hbar v_F}\right)^2\left(1 - \frac{\mu}{mv_F^2}\right) \quad (29)$$

from which it follows that

$$\mu \simeq \sqrt{4\pi n\hbar}v_F\left(1 + \frac{\sqrt{\pi n\hbar}}{mv_F}\right) \quad (30)$$

For $m = \infty$ we recover the known result for pure Dirac fermions $\mu = \sqrt{4\pi n\hbar}v_F$. For m not infinite, μ is increased over the pure relativistic limit value because of the change in the electronic dispersion curves. This increase in chemical potential is a direct consequence of the narrowing of the cross-section of the conduction band cone due to the subdominant Schrödinger term.

Returning to our approximate equations for $\mathcal{F}(N, +, +)$, $\mathcal{F}(N, +, -)$ and $\mathcal{F}(N, -, +)$ we note that in all cases the corrections for a non zero value of $1/P$ is of order $1/\sqrt{P}$ and more importantly, that the spectral weight associated with the interband transition remains finite even when $1/\sqrt{P} = 0$. This is in sharp contrast to what we found in the non-relativistic limit where they vanish when no subdominant Dirac correction is included. For the pure relativistic case the photon energy associated with both $(+, -)$ and $(-, +)$ interband transitions is the same. But here with $1/\sqrt{P} \neq 0$ the $(+, -)$ transition is slightly shorter than is the $(-, +)$ transition. We also see, noting the sign of

the thermal factors in Eq. (5), that the optical spectral weight associated with the larger photon energy has the smallest spectral weight. To first leading order in $1/\sqrt{P}$ however the total spectral weight under the two split lines is unchanged from the pure relativistic case where $1/\sqrt{P} = 0$. In graphene it is well known¹⁷ that as μ is increased so as to cross the N 'th LL line only one half the spectral weight remains in the N 'th line and all others for $n < N$ have disappeared with the entire spectral weight lost in the interband transition reappearing in the single intraband line which moves to lower photon energy with increasing μ and picks up more intensity. This sum rule on the redistribution of the spectral weight between inter and intra lines is encapsulated in the equation¹⁷

$$\sum_{n=0}^{N-1} \frac{2}{\sqrt{n+1} + \sqrt{n}} + \frac{1}{\sqrt{N+1} + \sqrt{N}} = \frac{1}{\sqrt{N+1} - \sqrt{N}} \quad (31)$$

derived in Ref [17], see their Eq. (33). The first term on the left is related to the spectral weight associated with all lines that have completely disappeared while the second is half of the spectral weight of the line $n = N$. The right hand side is the spectral weight in the intraband line. It is clear from our approximate Eq. (19-22) and Eq. (5) that this sum rule will no longer hold when $1/\sqrt{P} \neq 0$ since pairs of lines that have completely disappeared will have the same spectral weight as for the pure Dirac case while the one for $n = N$ will have a correction of order $1/\sqrt{P}$ (reduction) which does not match precisely the intraband correction of order $1/\sqrt{P}$.

Next we return to our numerical results of Fig. 6 which do not require the $1/\sqrt{P} \rightarrow 0$ limit and these show explicitly a change in optical sum with Schrödinger admixture. The first peak in each of the three top curves for $Re\sigma_{xx}(\omega)$ come from the intraband optical transitions while all other peaks are interband. As the Schrödinger contribution is increased through a decrease in m all intraband lines are seen to shift slightly to higher energies as compared to the pure Dirac case (which close to the $m = m_e$ curves). Also the optical spectral weight contained in the intraband line increases as the Schrödinger mass is decreased. This fact is more easily seen in the lower frame of Fig. 6 where we give results for $W(\omega)$ of Eq. (18) as a function of ω in meV with W in units of $\frac{e^2}{h}$ meV. All the curves start from zero and rise rapidly as we integrate over the intraband line after which it has a plateau which is nearly but not quite constant, followed by a more rapid rise modulated by small wiggles that reflect the LL structure. These wiggles would of course be more pronounced if we had reduced the broadening Γ . Here it is $15K$. The height of the first plateau in $W(\omega)$ gives the amount of spectral weight contained in the intraband transition and this clearly increase as we move further away from the pure relativistic case. Differences in $W(\omega)$ remain to high energies and these reflect the small Schrödinger admixture which we have added to the Hamiltonian.

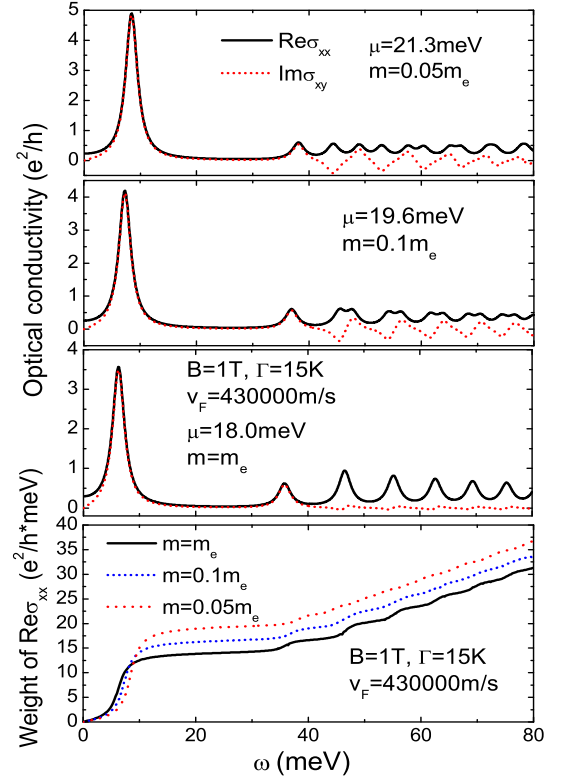


FIG. 6. (Color online) Top frame is the dynamic longitudinal $\sigma_{xx}(\omega)$ (solid black) and transverse $\sigma_{xy}(\omega)$ (Hall, dotted red) conductivity in units of e^2/h as a function of photon energy $\hbar\omega$ in meV. The Dirac fermi velocity is set at $v_F = 4.3 \times 10^5$ m/s which is nearly two orders of magnitude larger than used in the top frame of Fig. 3 and is representative of topological insulators. Top, second and third frames are for the Schrödinger mass equal to m_e , $0.1m_e$ and $0.05m_e$ respectively with m_e the bare electron mass. The bottom frame gives the optical spectral weight $W(\omega_c)$ in units of $e^2/h \times \text{meV}$ as a function of photon energy $\hbar\omega$ in meV. The curves are for $B = 1$ Tesla. The solid black is for $m = m_e$, dotted blue for $m = 0.1m_e$ and dotted red is for $m = 0.05m_e$.

V. REDISTRIBUTION OF SPECTRAL WEIGHT WITH μ

Next we return to the issue of how optical spectral weight gets redistributed between inter and intra band when the chemical potential μ is varied i.e. a change in doping, without assuming $1/\sqrt{P} \ll 1$. We begin with the case of $B = 0$ because in that instance, as we have seen, we can get analytic results. In previous sections we showed that the Drude weight is given by Eq. (16). Only the first line in this equation applies in the relativistic limit while both lines (Eq. (16)) contribute in the non-relativistic case. Further, we saw that the interband transition provide a constant background of $\frac{e^2\pi}{8h}$ in magnitude, with sharp absorption edge at ω_{\min} which terminates at ω_{\max} (see Eq. (14) and (15)). The total

optical spectral weight in this background is $4mv_F^2 \frac{e^2\pi}{8h}$. For comparison with the relativistic limit let us begin by computing the optical spectral weight that is missing from the universal background between $\omega = 0$ and $\omega = \omega_{\min}$. For $m \rightarrow \infty$ we can expand the expression for ω_{\min} and obtain to lowest order

$$\omega_{\max} \simeq 2\mu \left[1 - \frac{\mu}{2mv_F^2} \right] \quad (32)$$

which gives the known result that the interband absorption edge starts precisely at 2μ in the pure relativistic limit. When m is not infinite the absorption edge has shifted to an energy somewhat less than 2μ . The missing optical spectral weight is

$$\frac{e^2\pi}{8h} \times 2\mu \left[1 - \frac{\mu}{2mv_F^2} \right] \quad (33)$$

which is also somewhat less than $\frac{e^2\pi}{4h}\mu$ found in the limit $m = \infty$. Now in the limit of a topological insulator the Drude weight is given to leading order in an expansion for large m in Eq. (27) and is not equal to the missing weight in the universal background given in Eq. (33). So the spectral weight redistribution sum rule which is operative in the pure relativistic limit breaks down when a subdominant Schrödinger piece is added to the Hamiltonian.

The opposite limit (non-relativistic case) is also of interest. In that case both terms in the Eq. (16) need to be retained and to lowest order in v_F , W_D is given by Eq. (17). Further the missing weight in the universal background below the interband absorption edge is in the same approximation

$$\frac{e^2\pi}{4h} \sqrt{2m\mu} v_F \left[1 - \sqrt{\frac{mv_F^2}{2\mu}} \right] \quad (34)$$

which does not depend on μ in the same way as (17). It is clear that no sum rule applies in this limit as well. The pure relativistic case is unique and special.

Similar results hold when a magnetic field is present as we can see in Fig. 7 which gives the total spectral weight below ω ($W(\omega)$) under the real part of the longitudinal conductivity $Re\sigma_{xx}(\omega)$ in units of $(e^2/h) \times \text{meV}$ as a function of ω in meV. Four cases are shown with $B = 1$ Tesla, $\Gamma = 15K$, $v_F = 4.3 \times 10^5 \text{m/s}$ and the Schrödinger mass $m = 0.05m_e$. The four values of chemical potential are (solid black curve) $\mu = 29.1 \text{meV}$, (dashed green) $\mu = 35.7 \text{meV}$, (dashed dotted red) $\mu = 41.8 \text{meV}$ and (blue dots) $\mu = 47.4 \text{meV}$. For the first curve the open circles compare with the $B = 0$ case which starts at a finite value at $\omega = 0$ because we have assumed the clean limit and so the intraband transitions contribute a Dirac delta function to the frequency dependent conductivity. $W(\omega)$ then remains completely flat until the onset of the interband transitions set in at $\omega_{\min} = 47.8 \text{meV}$ given by Eq. (14). This is quite a lot smaller than the value of $2\mu \simeq 60 \text{meV}$. The curve for $B = 0$ follows well the solid

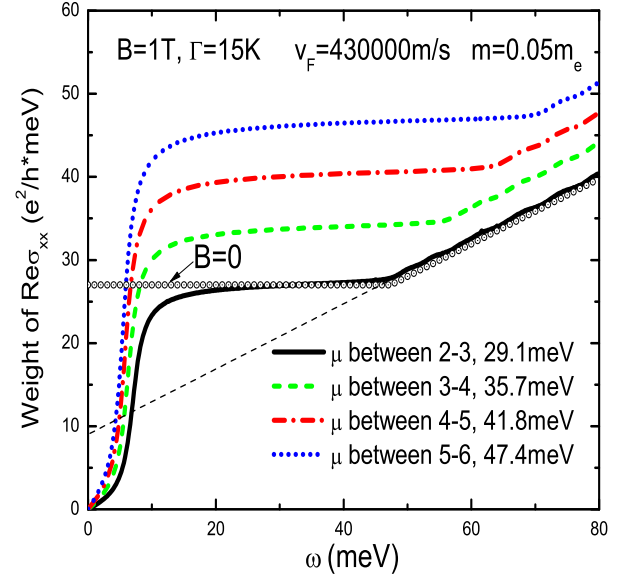


FIG. 7. (Color online) The partial optical spectral weight $W(\omega)$ to an upper cut off ω (in meV) for four values of chemical potential $\mu = 29.1 \text{ meV}$ (solid black curve), $\mu = 35.7 \text{ meV}$ (dashed green curve), $\mu = 41.8 \text{ meV}$ (dash-dotted red curve) and $\mu = 47.4 \text{ meV}$ (dotted blue curve). In all cases the magnetic field is $B=1$ Tesla, the Dirac fermi velocity is $4.3 \times 10^5 \text{ m/s}$ and the Schrödinger mass is $0.05m_e$. The open circles are for comparison with the solid black curve but now B is set to zero. The light dashed line extrapolates the straight line defined above the interband threshold in the solid black curve. Its intercept with the vertical axis is a measure of the deviation from pure Dirac behavior brought about by the presence of a subdominant Schrödinger piece in the Hamiltonian (1).

black curve for $B = 1T$ except of course that in this instance the Drude is replaced by the intraband peak and so $W(\omega)$ starts from zero at $\omega = 0$ and becomes equal to the black dots only after all the spectral weight in this line has been picked up. Above the interband onset both curves rise linearly with increasing ω with the slope of this line set by the value of the universal background. If we extrapolate it to $\omega = 0$ we find that it intercepts the $\omega = 0$ axis at a non zero value given by $\frac{e^2\pi}{8h}\omega_{\min}(A-1) \equiv \frac{e^2\pi}{4h}mv_F^2(A-1)^2$ with $A \equiv \sqrt{1 + \frac{2\mu}{mv_F^2}}$. For $m = \infty$, $A = 1$ and this intercept is equal to zero which applies only for the pure relativistic case. By contrast in topological insulators A is not one. Should one know independently the value of the chemical potential one could use the value of the intercept $\frac{e^2\pi}{4h}mv_F^2(A-1)^2$ to determine mv_F^2 which is a central parameter in assessing the deviations from the pure relativistic case expected in a given topological insulator. Note with reference to the lower frame in Fig. 6 that an extrapolation of the near linear region of the black curve for $m = m_e$, to $\omega = 0$ will give almost zero intercept and this reflect the fact that in this case the Schrödinger correction to pure Dirac is small.

Returning to the data in Fig. 7, $W(\omega)$ rises to a larger

magnitude for the plateau between the saturation of the intraband spectral weight and the threshold for the interband transition as the chemical potential is increased. This reflects the fact that as μ increases, more interband lines are lost because of Pauli blocking and some of their optical weight is transferred to the intraband line. The onset of the interband transition beyond the intraband plateau in $W(\omega)$ increases with increasing μ but the linear rise above this critical photon energy has the same slope in all cases. The small variations about a straight line seen in this region reflect of course the underlying Landau level structure which is smeared almost completely by the broadening $\Gamma = 15K$. At higher energies all the curves become parallel to each other but are displaced upward as μ is increased. In graphene, as can be seen in Fig. 7 of Ref. [17], the curves would all merge in this region in contrast to what we find here for topological insulators when the value of the subdominant Schrödinger part to the Hamiltonian is significant. It is the value of the intercept with the vertical axis of the straight line variation at large energies which sets the displacement between these parallel lines and as we have seen graphene corresponds to the limit of zero intercept.

VI. SUMMARY AND CONCLUSIONS

We have calculated the absorptive part of both longitudinal and transverse (Hall) AC dynamic magneto conductivity for quadratic electronic bands modified by a small spin orbit coupling. This provides a mechanism for interband optical transitions between the split helical bands. These optical transitions are additional to the main intraband (Drude) absorption which is the only process possible when the spin-orbit coupling is not present. We find that for the rather small values of Fermi velocity representative of the semiconductors presently used in spintronic applications, the interband absorption is small and that this background is likely not to be seen as distinct from the main Drude intraband absorption. However as the Fermi velocity v_F is increased a distinct interband background emerges which takes on the same universal values of $\frac{e^2\pi}{8h}$ as observed in graphene except for a degeneracy factor of 4 not applicable in this case. The universal background however is confined to a definite very limited range of photon energies with upper and lower cut off dependent on the value of the chemical potential and also on the magnitude of the magnetic field when B is also present. Comparison of these results with

those obtained in the opposite limit, when instead the Schrödinger term is a small perturbation on a dominant spin orbit term, provides new insight into the case of topological insulators. There, the interband transitions are much more prominent, extend to large energies and are cut off only by the band edge. For no magnetic field ($B = 0$) we were able to obtain analytic results which are valid for any value of m and v_F and these confirmed aspects of our finite B results. We showed that the interband background contains a total optical spectral weight of $\frac{e^2\pi}{8h}4mv_F^2$ which is independent of μ . This spectral weight is small when either m or v_F is small and it is large when both m and v_F are large as in topological insulators. In particular for $m \rightarrow \infty$ we recover the known result for graphene where only the Dirac contribution is present, and the interband transitions extend to the band cut off.

When the chemical potential μ is increased, a well known result for graphene is that all the optical spectral weight lost in the interband transitions is found transferred to the intraband transitions. This conservation of spectral weight no longer applies when a subdominant Schrödinger piece is added to a pure Dirac Hamiltonian. While these violations are small for typical parameters associated with present day known topological insulators, measuring them allows one to determine the critical parameter mv_F^2 which provides the information on the expected deviations of optical properties from the pure Dirac case. In the spintronic limit we find that the amount of spectral weight in the interband background is almost fixed while at the same time the intraband contribution increase with increasing chemical potential.

ACKNOWLEDGMENTS

This work was supported by the Natural Sciences and Engineering Research Council of Canada (NSERC) and the Canadian Institute for Advanced Research (CIFAR). This material is also based upon work supported by the National Science Foundation under the NSF EPSCoR Cooperative Agreement No. EPS-1003897 with additional support from the Louisiana Board of Regents.

REFERENCES

-
- * lizhou@mcmaster.ca
 - † carbotte@mcmaster.ca
 - ¹ M. Z. Hasan and C. L. Kane, Rev. Mod. Phys. **82**, 3045 (2010).
 - ² X.-L. Qi and S.-C. Zhang, Rev. Mod. Phys. **83**, 1057 (2011).
 - ³ J. Moore, Nature (London), **464**, 194 (2010).
 - ⁴ D. Hsieh et.al, Nature (London), **460**, 1101 (2009).
 - ⁵ J. Fabian, A. Matos-Abiague, C. Ertler, P. Stano and I. Žutić, Acta Physica Slovaca **57**, No. 4 and 5, 565 (2007)

- ⁶ I. Zutic, J. Fabian and S. Das Sarma, Rev. Mod. Phys. **76**, 323 (2004)
- ⁷ S. A. Wolf et. al., Science **294**, 1488 (2001).
- ⁸ S. Das Sarma, Ann. Sci. **84**, 516(2001).
- ⁹ D. D. Awschalom and J. M. Kikkawa, Phys. Today **52**(6), 33 (1999).
- ¹⁰ F. D. M. Haldane, Phys. Rev. Lett. **61**, 2015 (1988).
- ¹¹ V. P. Gusynin and S. G. Sharapov, Phys. Rev. B **73**, 245411 (2006).
- ¹² V. P. Gusynin and S. G. Sharapov, Phys. Rev. Lett **95**, 146801 (2005).
- ¹³ Novoselov et.al, Nature **438**, 197 (2005).
- ¹⁴ X. Zhang, Y.-W. Tan, H. L. Stormer and P. Kim, Nature **438**, 201 (2005).
- ¹⁵ C.-X. Liu, X.-L. Qi, H. J. Zhang, X. Dai, Z. Fang and S.-C. Zhang, Phys. Rev. B **82**, 045122 (2010).
- ¹⁶ Zhou Li and J. P. Carbotte, Phys. Rev. B **89**, 085413 (2014).
- ¹⁷ V. P. Gusynin, S. G. Sharapov and J. P. Carbotte, J. Phys.: Condens. Matter **19**, 026222 (2007).
- ¹⁸ V. P. Gusynin, S. G. Sharapov and J. P. Carbotte, Phys. Rev. Lett. **98**, 157402 (2007).
- ¹⁹ A. Pound, J. P. Carbotte and E. J. Nicol, Phys. Rev. B **85**, 125422 (2012).
- ²⁰ M. L. Sadowski, G. Martinez, M. Potemski, C. Berger and W. A. de Heer, Solid State Communi. **143**, 123 (2007).
- ²¹ Z. Jiang et.al, Phys. Rev. Lett. **98**, 197403 (2007).
- ²² R. S. Deacon, K.-C. Chuang, R. J. Nicholas, K. S. Novoselov and A. K. Geim, Phys. Rev. B **76**, 081406 (2007).
- ²³ M. Orlita and M. Potemski, Semicond. Sci. Technol. **25**, 063001 (2010).
- ²⁴ C. J. Tabert and E. J. Nicol, Phys. Rev. Lett. **110**, 197402 (2013).
- ²⁵ C. J. Tabert and E. J. Nicol, Phys. Rev. B **88**, 085434 (2013).
- ²⁶ Zhou Li and J. P. Carbotte, Phys. Rev. B **88**, 045414 (2013).
- ²⁷ W.-K. Tse and A. H. MacDonald, Phys. Rev. B **84**, 205327 (2011).
- ²⁸ A. A. Schafgans, K. W. Post, A. A. Taskin, Y. Ando, X.-L. Qi, B. C. Chapler and D. N. Basov, Phys. Rev. B **85**, 195440 (2012).
- ²⁹ F. Rose, M. O. Goerbig and F. Piechon, Phys. Rev. B **88**, 125438 (2013).
- ³⁰ P. E. C. Ashby and J. P. Carbotte, Phys. Rev. B **87**, 245131 (2013).
- ³¹ Y. L. Chen et.al. Science **329**, 659 (2010).
- ³² S.-Y. Xu, X Xia et.al, Science **332**, 560 (2011).
- ³³ Y. L. Chen et.al. Science **325**, 178 (2009).
- ³⁴ D. Hsieh et.al, Nature (London), **460**, 1101 (2009).
- ³⁵ W.-K. Tse and A. H. MacDonald, Phys. Rev. Lett. **105**, 057401 (2010).
- ³⁶ W.-K. Tse and A. H. MacDonald, Phys. Rev. B. **82**, 161104(R) (2010).
- ³⁷ G. Tkachov and E. M. Hankiewicz, Phys. Rev. B. **83**, 155412 (2011).
- ³⁸ G. Tkachov and E. M. Hankiewicz, Phys. Rev. B. **84**, 035405 (2011).
- ³⁹ D. S. L. Abergel and Vladimir I. Falko, Phys. Rev. B. **75**, 155430 (2007).
- ⁴⁰ Mikito Koshino and Tsuneya Ando, Phys. Rev. B. **77**, 115313 (2008).

- ⁴¹ Benedikt Scharf, Vasili Perebeinos, Jaroslav Fabian, and Igor Žutić, Phys. Rev. B. **88**, 125429 (2013).
- ⁴² Y. Kim et.al., Phys. Rev. Lett. **110**, 227402 (2013).

Appendix A: Derivation of the Drude spectral weight at zero magnetic field

The Hamiltonian is given by Eq. (1) and here we write $\alpha = \hbar v_F$.

$$H_0 = \frac{\hbar^2 k^2}{2m} + \alpha(k_x \sigma_y - k_y \sigma_x) \quad (\text{A1})$$

The velocity is

$$\begin{aligned} v_x &= \frac{\partial H_0}{\partial k_x} = \frac{\hbar^2 k_x}{m} + \alpha \sigma_y = v_D I + \alpha \sigma_y, \\ v_y &= \frac{\partial H_0}{\partial k_y} = \frac{\hbar^2 k_y}{m} - \alpha \sigma_x = v_D I - \alpha \sigma_x. \end{aligned}$$

The matrix Green's function can be expanded in matrix spectral function $\hat{A}(\mathbf{k}, \omega)$ as

$$\hat{G}(\mathbf{k}, z) = \int_{-\infty}^{\infty} \frac{d\omega}{2\pi} \frac{\hat{A}(\mathbf{k}, \omega)}{z - \omega} \quad (\text{A2})$$

The conductivity $\sigma_{xx}(\omega)$ is given by

$$\begin{aligned} \sigma_{xx}(\omega) &= -\frac{e^2}{i\omega} \int_{-\infty}^{\infty} \frac{d\omega_1}{2\pi} \int_{-\infty}^{\infty} \frac{d\omega_2}{2\pi} \frac{[f(\omega_1) - f(\omega_2)]}{\omega - \omega_2 + \omega_1 + i\delta} \\ &\quad \sum_{\mathbf{k}} \text{Tr} \langle v_x \hat{A}(\mathbf{k}, \omega_1) v_x \hat{A}(\mathbf{k}, \omega_2) \rangle \end{aligned} \quad (\text{A3})$$

and the real part of the conductivity at zero temperature is given by

$$\begin{aligned} \text{Re} \sigma_{xx}(\omega) &= \frac{e^2}{2\omega} \frac{1}{4\pi^2} \int_0^{k_{cut}} k dk d\theta \int_{-\omega}^0 \frac{d\omega_1}{2\pi} \\ &\quad \text{Tr} \langle v_x \hat{A}(\mathbf{k}, \omega_1) v_x \hat{A}(\mathbf{k}, \omega + \omega_1) \rangle \end{aligned} \quad (\text{A4})$$

The spectral function is the imaginary part of the Green's function

$$\hat{A}(\mathbf{k}, x) = -2\text{Im} \hat{G}(\mathbf{k}, x) \quad (\text{A5})$$

The Green's function is given by

$$\hat{G}_0(\mathbf{k}, i\omega_n) = \frac{1}{2} \sum_{s=\pm} (1 + s \mathbf{F}_k \cdot \boldsymbol{\sigma}) G_0(\mathbf{k}, s, i\omega_n) \quad (\text{A6})$$

where

$$\mathbf{F}_k = \frac{(-k_y, k_x, 0)}{k} \quad (\text{A7})$$

and

$$G_0(\mathbf{k}, s, i\omega_n) = \frac{1}{i\omega_n + \mu - \frac{\hbar^2 k^2}{2m} - s\alpha k} \quad (\text{A8})$$

After taking the trace we get

$$\begin{aligned}
& Re\sigma_{xx}(\omega) \\
&= \frac{e^2}{4\omega} \int_0^{k_{cut}} k dk \int_{-\omega}^0 \frac{d\omega_1}{2\pi} \\
& \quad 2\pi\alpha^2 [\delta(\widetilde{\omega}_1 - \alpha k)\delta(\widetilde{\omega}_2 - \alpha k) + \delta(\widetilde{\omega}_1 + \alpha k)\delta(\widetilde{\omega}_2 + \alpha k) \\
& \quad + \delta(\widetilde{\omega}_1 + \alpha k)\delta(\widetilde{\omega}_2 - \alpha k) + \delta(\widetilde{\omega}_1 - \alpha k)\delta(\widetilde{\omega}_2 + \alpha k)] \\
& \quad + 2\pi \frac{\hbar^4 k^2}{m^2} [\delta(\widetilde{\omega}_1 - \alpha k)\delta(\widetilde{\omega}_2 - \alpha k) + \delta(\widetilde{\omega}_1 + \alpha k)\delta(\widetilde{\omega}_2 + \alpha k)] \\
& \quad + 4\pi\alpha \frac{\hbar^2 k}{m} [\delta(\widetilde{\omega}_1 - \alpha k)\delta(\widetilde{\omega}_2 - \alpha k) - \delta(\widetilde{\omega}_1 + \alpha k)\delta(\widetilde{\omega}_2 + \alpha k)]
\end{aligned}$$

where

$$\widetilde{\omega}_1 = \omega_1 + \mu - \frac{\hbar^2 k^2}{2m} \quad (A9)$$

$$\widetilde{\omega}_2 = \omega_1 + \omega + \mu - \frac{\hbar^2 k^2}{2m} \quad (A10)$$

The term with $\delta(\widetilde{\omega}_1 + \alpha k)\delta(\widetilde{\omega}_2 - \alpha k)$ and $\delta(\widetilde{\omega}_1 - \alpha k)\delta(\widetilde{\omega}_2 + \alpha k)$ will be zero for topological insulator but nonzero for spintronics. For topological insulators we have for $\mu > 0, \omega_1 \simeq 0, \omega_1 + \mu - \frac{\hbar^2 k^2}{2m} - \alpha k = 0 \Rightarrow k = \frac{m}{\hbar^2}[-\alpha + \sqrt{\alpha^2 + 2\hbar^2/m(\omega_1 + \mu)}]$, and

$$\begin{aligned}
& \int_0^{k_{cut}} dk \cdot k \delta(\widetilde{\omega}_1 - \alpha k)\delta(\widetilde{\omega}_2 - \alpha k) \\
&= \frac{m - \alpha + \sqrt{\alpha^2 + 2\hbar^2/m(\omega_1 + \mu)}}{\hbar^2} \delta(\omega) \quad (A11)
\end{aligned}$$

$$\begin{aligned}
& \int_0^{k_{cut}} dk \cdot k^2 \delta(\widetilde{\omega}_1 - \alpha k)\delta(\widetilde{\omega}_2 - \alpha k) \\
&= \left(\frac{m}{\hbar^2}\right)^2 \frac{(-\alpha + \sqrt{\alpha^2 + 2\hbar^2/m(\omega_1 + \mu)})^2}{\sqrt{\alpha^2 + 2\hbar^2/m(\omega_1 + \mu)}} \delta(\omega) \quad (A12)
\end{aligned}$$

$$\begin{aligned}
& \int_0^{k_{cut}} dk \cdot k^3 \delta(\widetilde{\omega}_1 - \alpha k)\delta(\widetilde{\omega}_2 - \alpha k) \\
&= \left(\frac{m}{\hbar^2}\right)^3 \frac{(-\alpha + \sqrt{\alpha^2 + 2\hbar^2/m(\omega_1 + \mu)})^3}{\sqrt{\alpha^2 + 2\hbar^2/m(\omega_1 + \mu)}} \delta(\omega) \quad (A13)
\end{aligned}$$

For $\mu < 0, \omega_1 \simeq 0, \omega_1 + \mu - \frac{\hbar^2 k^2}{2m} + \alpha k = 0 \Rightarrow k_0 = \frac{m}{\hbar^2}[\alpha - \sqrt{\alpha^2 + 2\hbar^2/m(\omega_1 + \mu)}]$. Because $k_{cut} = \frac{m\alpha}{\hbar^2}$ and the energy at this point $E_{\min} = \frac{-m\alpha^2}{2\hbar^2}$. The delta function can be rewritten as $\delta(\widetilde{\omega}_1 + \alpha k) = \frac{\delta(k - k_0)}{|f'(k_0)|}$, where

$$\begin{aligned}
|f'(k_0)| &= |-\frac{\hbar^2 k_0}{m} + \alpha| = \sqrt{\alpha^2 + 2\hbar^2/m(\omega_1 + \mu)}. \text{ Thus} \\
& \int_0^{k_{cut}} dk \cdot k \delta(\widetilde{\omega}_1 + \alpha k)\delta(\widetilde{\omega}_2 + \alpha k) \\
&= \frac{m}{\hbar^2} \frac{\alpha - \sqrt{\alpha^2 + 2\hbar^2/m(\omega_1 + \mu)}}{\sqrt{\alpha^2 + 2\hbar^2/m(\omega_1 + \mu)}} \delta(\omega) \quad (A14)
\end{aligned}$$

$$\begin{aligned}
& \int_0^{k_{cut}} dk \cdot k^2 \delta(\widetilde{\omega}_1 + \alpha k)\delta(\widetilde{\omega}_2 + \alpha k) \\
&= \left(\frac{m}{\hbar^2}\right)^2 \frac{(\alpha - \sqrt{\alpha^2 + 2\hbar^2/m(\omega_1 + \mu)})^2}{\sqrt{\alpha^2 + 2\hbar^2/m(\omega_1 + \mu)}} \delta(\omega) \quad (A15)
\end{aligned}$$

$$\begin{aligned}
& \int_0^{k_{cut}} dk \cdot k^3 \delta(\widetilde{\omega}_1 + \alpha k)\delta(\widetilde{\omega}_2 + \alpha k) \\
&= \left(\frac{m}{\hbar^2}\right)^3 \frac{(\alpha - \sqrt{\alpha^2 + 2\hbar^2/m(\omega_1 + \mu)})^3}{\sqrt{\alpha^2 + 2\hbar^2/m(\omega_1 + \mu)}} \delta(\omega) \quad (A16)
\end{aligned}$$

and hence

$$\begin{aligned}
& \int_{-\omega}^0 d\omega_1 \frac{\alpha - \sqrt{\alpha^2 + 2\hbar^2/m(\omega_1 + \mu)}}{\sqrt{\alpha^2 + 2\hbar^2/m(\omega_1 + \mu)}} \\
&= \frac{\alpha\omega}{\sqrt{\alpha^2 + (2\hbar^2/m)\mu}} - \omega
\end{aligned}$$

Similarly

$$\begin{aligned}
& \int_{-\omega}^0 d\omega_1 \frac{(\alpha - \sqrt{\alpha^2 + 2\hbar^2/m(\omega_1 + \mu)})^2}{\sqrt{\alpha^2 + 2\hbar^2/m(\omega_1 + \mu)}} \\
&= \frac{(\alpha - \sqrt{\alpha^2 + (2\hbar^2/m)\mu})^2 \omega}{\sqrt{\alpha^2 + (2\hbar^2/m)\mu}}
\end{aligned}$$

and

$$\begin{aligned}
& \int_{-\omega}^0 d\omega_1 \frac{(\alpha - \sqrt{\alpha^2 + 2\hbar^2/m(\omega_1 + \mu)})^3}{\sqrt{\alpha^2 + 2\hbar^2/m(\omega_1 + \mu)}} \\
&= \frac{(\alpha - \sqrt{\alpha^2 + (2\hbar^2/m)\mu})^3 \omega}{\sqrt{\alpha^2 + (2\hbar^2/m)\mu}}
\end{aligned}$$

Thus for $\mu < 0$,

$$Re\sigma_{xx}(\omega) = \frac{e^2 m (\alpha - \sqrt{\alpha^2 + (2\hbar^2/m)\mu}) \sqrt{\alpha^2 + (2\hbar^2/m)\mu}}{4\hbar^2} \delta(\omega) \quad (A17)$$

and for $\mu > 0$,

$$Re\sigma_{xx}(\omega) = \frac{e^2 m (\sqrt{\alpha^2 + (2\hbar^2/m)\mu} - \alpha) \sqrt{\alpha^2 + (2\hbar^2/m)\mu}}{4\hbar^2} \delta(\omega) \quad (A18)$$

For spintronics we can perform similar algebra.